Earth and Planetary Science Letters 543 (2020) 116312

Contents lists available at ScienceDirect

Earth and Planetary Science Letters

www.elsevier.com/locate/epsl

The early Eocene rise of the Gonjo Basin, SE Tibet: From low desert to high forest

Zhongyu Xiong [a,b], Lin Ding [a,*], Robert A. Spicer [c,d], Alexander Farnsworth [e], Xu Wang [f], Paul J. Valdes [e], Tao Su [c], Qinghai Zhang [a], Liyun Zhang [a], Fulong Cai [a], Houqi Wang [a], Zhenyu Li [a], Peiping Song [a], Xudong Guo [a], Yahui Yue [a]

[a] Key laboratory of Continental Collision and Plateau Uplift, Institute of Tibetan Plateau Research, and Center for Excellence in Tibetan Plateau Earth Sciences, Chinese Academy of Sciences, Beijing 100101, China
[b] College of Resources and Environment, University of Chinese Academy of Sciences, Beijing 100049, China
[c] CAS Key Laboratory of Tropical Forest Ecology, Xishuangbanna Tropical Botanical Garden, Chinese Academy of Sciences, Mengla 666303, China
[d] School of Environment, Earth and Ecosystem Sciences, The Open University, Milton Keynes MK76AA, UK
[e] School of Geographical Sciences, University of Bristol, University Road, Clifton, Bristol BS8 1SS, UK
[f] Key Laboratory of Cenozoic Geology and Environment, Institute of Geology and Geophysics, Chinese Academy of Sciences, Beijing 100101, China

ARTICLE INFO

Article history:
Received 2 November 2019
Received in revised form 23 April 2020
Accepted 27 April 2020
Available online 26 May 2020
Editor: A. Yin

Keywords:
SE Tibetan Plateau
clumped isotope
paleoelevation
Eocene
intracontinental subduction

ABSTRACT

Views differ on the uplift history of the SE Tibetan Plateau and causal geodynamic mechanisms, yet reliable age-constrained paleoaltimetry in this region could test growth models of the entire plateau. Here we apply carbonate clumped isotope thermometry to well-dated carbonate paleosols and marls in the Gonjo Basin, SE Tibet, to reveal the topographic evolution of the basin. The sedimentary ages of carbonates of the lower and upper Ranmugou Formation are constrained to 54-50 Ma and 44-40 Ma, respectively. The temperature derived from carbonate clumped isotope thermometry indicates the mean annual air temperature (MAAT) of the Gonjo Basin in the early Eocene was ~24 °C, which is consistent with the warm climate indicated by palm fossils. The MAAT of the basin in the middle Eocene was ~7 °C, 17 °C cooler than in the early Eocene. Carbonate clumped oxygen isotope thermometry-based paleoaltimetry shows the Gonjo Basin experienced a rapid uplift of 3.1 km, from ~0.7 km in the early Eocene to ~3.8 km in the middle Eocene. This rise explains the marked cooling. As a cause of this rapid rise, and the associated regional climate change transforming the landscape from desert to forest, we invoke crustal deformation and thickening induced by intracontinental subduction between the Lhasa and Qiangtang terranes that comprise the core of the Tibet.

1. Introduction

The long-wavelength, low-gradient ramp-like topography of the SE edge of the Tibetan Plateau is distinct from the other precipitous margins of the plateau (Clark and Royden, 2000), and the tectonic mechanism producing this distinctive margin has long been debated. One idea suggests that the SE Tibetan Plateau attained its present topographic relief through continental extrusion along major strike-slip faults after 55 Ma (Tapponnier et al., 2001). This hypothesis of continental extrusion is mainly based on geologic observations of large-scale strike slip offsets along the Ailaoshan-Red River, Chongshan and Gaoligong Shear Zones (Fig. 1a) (Searle, 2006; Xu et al., 2015). An alternative model envisages middle or lower crustal flow from the already thickened crust in central plateau during the late Miocene (Clark and Royden, 2000). This view is based on the observed gentle gradient in topography, crustal thickness (Clark et al., 2005) and crustal rheology modeling results (Royden et al., 2008), yet the Miocene interpretation is highly dependent on existing regional geochronology being correct and evidence is emerging that it is not and that a number of Cenozoic basins in SE Tibet were formed much earlier in the early Oligocene or Eocene (e.g. Gourbet et al., 2017; Linnemann et al., 2017; Su et al., 2018). Moreover, crustal shortening and thickening resulting from intracontinental subduction and deformation during the early Cenozoic India-Asia collision has also been cited as the cause of uplift (Ding et al., 2007; Spurlin et al., 2005; Yin and Harrison, 2000). This hypothesis is supported by the contractional structure and magmatic activities in the Qiangtang Terrane (Ding et al., 2007; Spurlin et al., 2005), and extensive amounts of de-

* Corresponding author.
E-mail address: dinglin@itpcas.ac.cn (L. Ding).

https://doi.org/10.1016/j.epsl.2020.116312

formation and shortening in the Tengchong and Baoshan terranes during the early Paleogene (Deng et al., 2014; Zhang et al., 2017).

The orographic development of the SE Tibetan Plateau has been studied in several basins to try and distinguish between the different tectonic models. The paleoelevation of the Markam Basin (Fig. 1a) derived from leaf fossil physiognomy suggests that the basin had reached its near-present elevation since by at least the late Eocene (Fig. 1a)(Su et al., 2018), which is consistent with coeval pervasive crustal shortening and igneous activities within the Qiangtang Terrane (Horton et al., 2002; Kapp et al., 2005; Spurlin et al., 2005). Oxygen isotope paleoaltimetry indicates that the Liming and Jianchuan basins (Fig. 1a) had risen to their present elevation by the Eocene, the Lanping and Eryuan basins (Fig. 1a) located in the south reached their present elevation by the middle Miocene, while the Chake Basin remained near sea level throughout the Eocene (Hoke et al., 2014). These results indicate that Tibetan orography has expanded southeastwards since the Eocene and exclude late Miocene lower crustal flow as the sole driver for uplift. However, the absolute sedimentary ages of numerous basins, such as Liming, Lanping and Eryuan basins in SE Tibet are still controversial (Gourbet et al., 2017), and because previous paleoelevation work used imprecise age constraints, the paleoelevation results (Hoke et al., 2014; Li et al., 2015; Tang et al., 2017) must remain questionable. Additionally, some of the carbonate samples used to determine the paleoelevations of these basins may have been diagenetically altered because no valid evidence was provided to indicate that these samples contained primary oxygen isotopic signatures (Hoke et al., 2014; Li et al., 2015; Tang et al., 2017). Given the uncertainties surrounding the age of the material, and the pristine nature of the isotopic signals, new accurate paleoelevations derived from primary pedogenic carbonates with well-constrained ages are required to shed light on the uplift mechanism and topographic evolution of the SE Tibet.

Here, to provide new constraints on the uplift history and the related tectonic process of this region, we present new zircon U-Pb ages from volcanic rocks and sandstones, plant fossil data, and stable and clumped isotope results of paleosol nodules and lacustrine marls that retain primary isotopic signatures from the Gonjo Basin, SE Tibetan Plateau. Furthermore, we supplement the isotopic results with a novel Lutetian age isotope-enabled climate model simulation to verify, quantitatively, the moisture sources and moisture trajectories underpinning our isotopic paleoaltimetry. The resultant paleoelevations indicate that the Gonjo Basin experienced a rapid uplift between the early and middle Eocene. Combined with previously published elevations in the Qiangtang Terrane, our results suggest that the Central Watershed mountain range in the Qiangtang Terrane (Fig. 1a), which divides the drainages feeding to the Indian Ocean from those flowing to the Pacific Ocean, experienced rapid uplift in the Eocene. We further suggest that Eocene uplift within the Qiangtang Terrane was driven by crustal deformation and thickening initiated by intracontinental subduction between the Lhasa and Qiangtang terranes. Moreover, uplift within the Qiangtang Terrane also changed substantially the climate and vegetation of the region.

2. Geological setting and sedimentology

The SE Tibetan Plateau consists of several continental fragments, including parts of the Lhasa, Qiangtang, Songpan-Ganzi and Yangzte terranes, the Yidun arc, and the Tengchong, Baoshan and Lanaping-Simao terranes (Fig. 1a) (Burchfiel and Chen, 2012). During the early stage of the India-Asia collision in the Paleogene, collision-related contractional deformation and magmatism occurred immediately in the Qiangtang Terrane (Ding et al., 2007; Kapp et al., 2005; Spurlin et al., 2005).

The NW-SE-oriented Gonjo Basin, located within the eastern Qiangtang Terrane, covers roughly 1870 km^2 and has an average elevation of ~4.0 km. The basin presents as a narrow, elongated syncline controlled by basin-bounding reverse faults on both east and west sides (Fig. 1b). Small scale reverse faults and strike slip faults developed after sedimentation began in the basin (Studnicki-Gizbert et al., 2008). The depositional basement of the Gonjo Basin includes both Paleozoic and Mesozoic units. The Cenozoic strata in the basin were thrusted by Triassic strata in the east and Carboniferous-Triassic strata in the west. Depositional contacts were also observed in some places near the western boundary (Fig. 1b). Cenozoic strata include the Gonjo Formation (E_1g) and the Ranmugou Formation (E_2r). The E_1g is conformably overlain by the E_2r. We measured four stratigraphic sections, namely the Shenda and G317 Highway sections in the northern basin, the Zongqing section in the central basin, and the Qudeng section in the southern basin (Fig. 1b). The lithologies are summarized below and detailed in the supplementary materials.

The E_1g consists of two different lithological units. The basal strata of the E_1g outcrop in the middle part of the basin are characterized by approximately 60 m of white to purple, coarse- to medium-grained, well-sorted sandstones that contain large, meter-scale, high angle cross-bedding (Fig. 2a, 3a). The quartz grains selected from the sandstone present well-rounded concavities (Fig. 2a_1–a_3). These characteristics indicate that the lower part of the E_1g formed in an eolian environment (Schenk and Fryberger, 1988). The upper beds of the measured E_1g are about 400 m in thickness, and are composed of claret-colored, pebbly sandstones at the base that fine upward to thinly bedded fine- to very fine-grained sandstones and siltstones. We interpret the sedimentary environment of the upper part of the E_1g as predominantly fluvial (Friedman and Sanders, 1978).

The E_2r is divided into two distinct lithological units, the lower Ranmugou Formation (E_2r_1), which is an assemblage of massive to layered conglomerates interbedded with sandstones and mudstones, and the upper Ranmugou Formation (E_2r_2), which is an assemblage consisting of planar upward-fining sandstones to mudstones interbedded with several layers of limestone or marl.

The conglomerate units in the E_2r_1 consist of red- to claret-colored, medium- to thick-bedded, pebble to cobble clast-supported conglomerates interbedded with thinner coarse sandstones, and fine upward to siltstones and mudstones (Fig. 3). The thicknesses range from 100 m to 600 m in our measured sections (Fig. 3). Gravel beds usually have erosive bottoms and clast imbrications (Fig. 2b). The thinner sandstones consist of purple to red, planar or lenticular, medium-bedded, well sorted, fine to coarse sandstones with some layers bearing cross-bedding. Paleosol horizons developed in the upward-fining sandstone and mudstone layers, with some paleosol exhibiting scour marks on their tops (Fig. 2b). Paleosol carbonate occurs as discrete nodules, 1-5 cm in diameter (Fig. 2c, 2d), usually in the lower half of paleosol horizon. Palm fossils were discovered in the fine-grained sandstone layer of the upper E_2r_1 in the Zongqing section (Fig. 2e). We interpret these facies as distal alluvial fan or fluvial (Friedman and Sanders, 1978).

The E_2r_2 mainly consists of two lithologic parts, the lower part consists of red- to claret-colored, rhythmic layers of thinly bedded, fine- to very fine-grained sandstones, siltstones and mudstones, the upper part consists of varicolored, thinly-bedded siltstones and mudstones with the uppermost beds interbedded with several layers of limestone or marl (Fig. 2f, 3). Beds comprising E_2r_2 are typically planar, exhibit ripple marks in some fine sandstones, and mud cracks in some mudstones (Fig. 2f). We interpret the E_2r_2 as representing lacustrine deposition (Friedman and Sanders, 1978). A variety of dateable volcanic rocks and sandstones, including tuffites and andesites, are present in the E_2r succession of the Shenda,

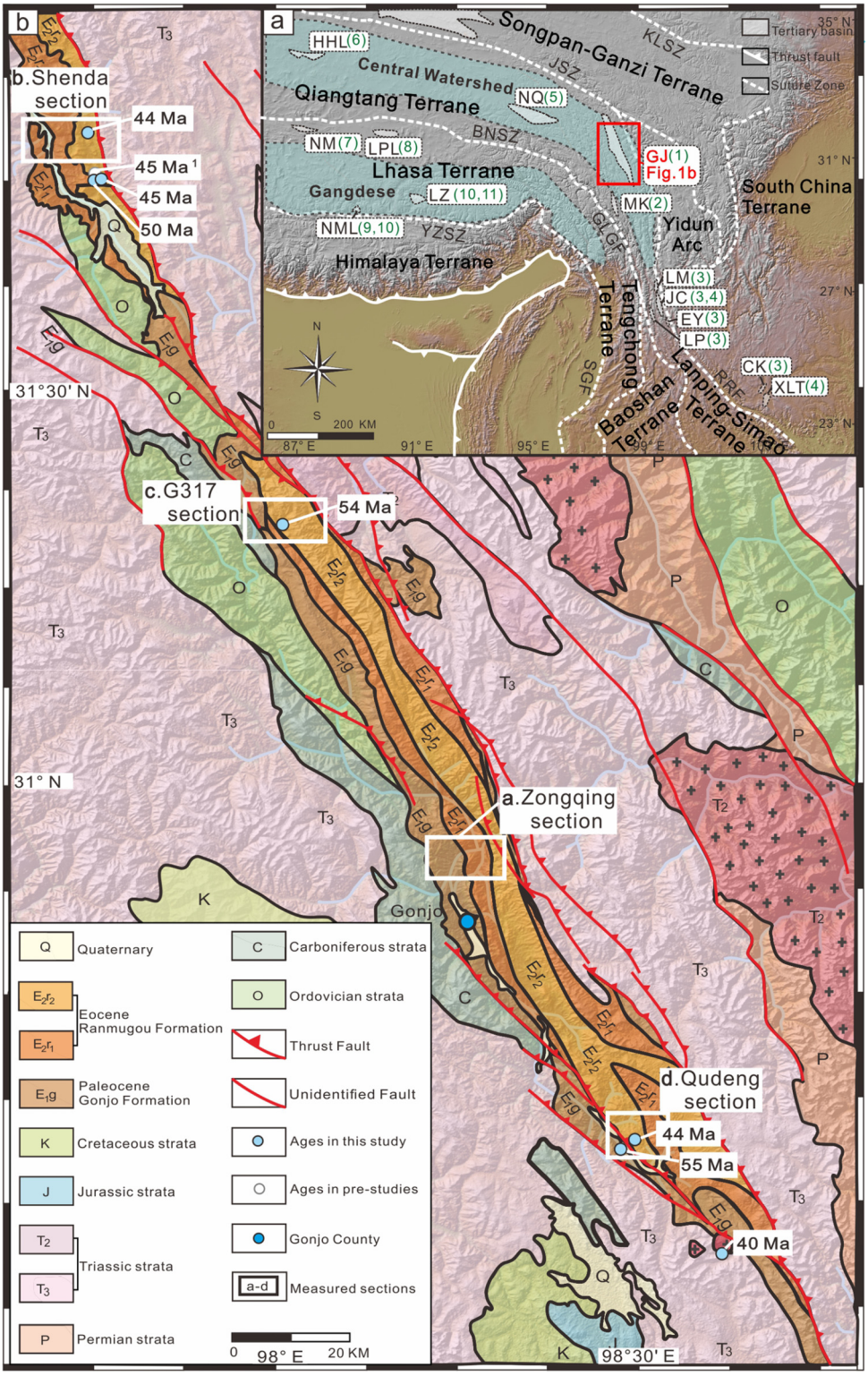

Fig. 1. (a) Topographic map of the SE Tibetan Plateau with previous paleoelevation data (modified from Burchfield and Chen, 2012). The red rectangle represents the location of the Gonjo Basin. Dashed lines represent suture zones bounding different terranes. The blue shaded area in the Qiangtang Terrane represents the Central Watershed mountain range, and the blue shaded area in the Lhasa Terrane represents the Gangdese mountain range. Abbreviations: BNSZ = Bangong-Nujiang Suture Zone, CK = Chake Basin, EY = Eryuan Basin, GJ = Gonjo Basin, GLGF = Gaoligong Fault, HHL = Heihuling Basin, HX = Hoh Xil Basin, JC = Jianchuan Basin, JSZ = Jingsha Suture Zone, KLSZ = Kunlun Suture Zone, LM = Liming Basin, LP = Lanping Basin, LPL = Lunpola Basin, LZ = Linzhou Basin, NM = Nima Basin, NML = Namling Basin, NQ = Nangqian Basin, MK = Markam Basin, RRF = Red River Fault, SGF =Saging Fault, XLT = Xiaolongtan Basin, YZSZ = Yalung-Zangpo Suture Zone. Plaoelevations and references: (1) GJ = 2.1-2.5 km (45 Ma) (Tang et al., 2017); (2) MK = 3.9 km (33-36) Ma (Su et al., 2018); (3) EY = 2.8 km (5-3 Ma), JC = 3.3 km (37-34 Ma), LM = 2.5 km (56-34 Ma), LP = 3.3 km (12-5 Ma) (Hoke et al., 2014)); (4) JC = 3.3 km (37-34 Ma), XLT = 1.6 km (23-16 Ma) (Li et al., 2015); (5) NQ = 3.0 km (40-37 Ma) (Li et al., 2018); (6) HHL = 5.0 km (51-28 Ma) (Xu et al., 2013); (7) NM = 4.0 km (26 Ma) (DeCelles et al., 2007); (8) LPL = 2.3 km (30 Ma) (Su et al., 2019); (9) NML = 5.2 km (15 Ma) (Spicer et al., 2003); (10) LZ = 4.4-4.1 km (60-48 Ma) (Ingalls et al., 2018); (11) LZ = 4.5 km (60-48 Ma) (Ding et al., 2014). (b) Geologic map of the Gonjo Basin (modified from Studnicki-Gizbert et al., 2008; Tang et al., 2017). Light blue circles show locations where U-Pb ages of zircon grains were obtained from volcanic rocks (this study), and grey circles indicate the data from a previous study (Tang et al., 2017). Gonjo county is shown as dark blue circle. The measured sections a-d denote the Zongqing section, Shenda section, G317 Highway section and Qudeng section, respectively. (For interpretation of the colors in the figure(s), the reader is referred to the web version of this article.)

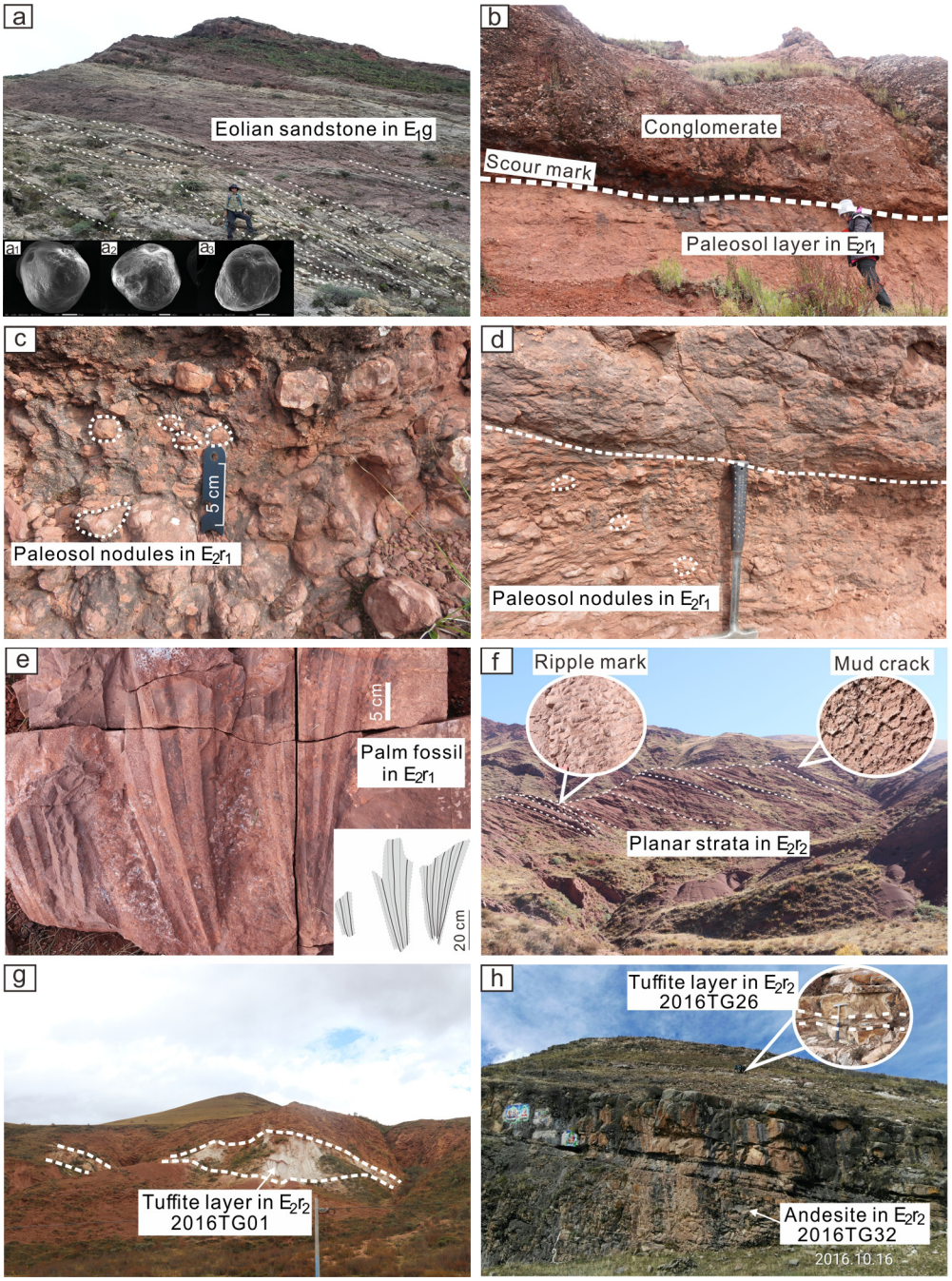

Fig. 2. Field photos showing outcrops of the E_1g and E_2r in the Gonjo Basin. (a) Eolian sandstone of E_1g from the Zongqing section, inserted pictures (a_1, a_2, a_3) show the round quartz grains with low relief and bulbous edges. (b) Paleosol layer in E_2r_1 with scour marks developed on the top from the Zongqing section. (c) Paleosol nodules in E_2r_1 from the Zongqing section. (d) Paleosol nodules in E_2r_1 from the G317 section. (e) The palm fossil in E_2r_1 from the Zongqing section. (f) Planar strata of E_2r_2 with ripple marks in sandstones and mud cracks in mudstones in the Zongqing section. (g) A tuffite layer in E_2r_2 (2016TG01) sampled for U-Pb zircon dating from the Qudeng Section. (h) Volcanic rocks interbedded with a tuffite layer in E_2r_2 (2016TG26, 32) sampled for U-Pb zircon dating from the Shenda section.

G317 and Qudeng sections (Fig. 2g, 2h), while granite intruded the southern Cenozoic strata of the basin.

3. Materials and analytical methods

3.1. Zircon U-Pb geochronology

Zircon crystals were separated from volcanic and sandstone samples, and analyzed on a New Wave UP 193FX Excimer laser (New Wave Instrument, USA) coupled to an Agilent 7500a inductively coupled plasma mass spectrometer (LA-ICP-MS) at the Key laboratory of Continental Collision and Plateau Uplift, Institute of Tibetan Plateau Research, Chinese Academy of Sciences (refer to supplementary materials for laboratory analysis methods and data deduction details).

3.2. Leaf fossil identification

One large fragmental palm leaf fossil was collected from the E_2r_1 in the Zongqing section (Fig. 2e) and identified in the Key Laboratory of Tropical Forest Ecology, Xishuangbanna Tropical Botanical Garden, Chinese Academy of Sciences. The morphology of the palm leaf was compared with extant relatives in a world palm database (palmweb.org) to estimate the lowest thresholds

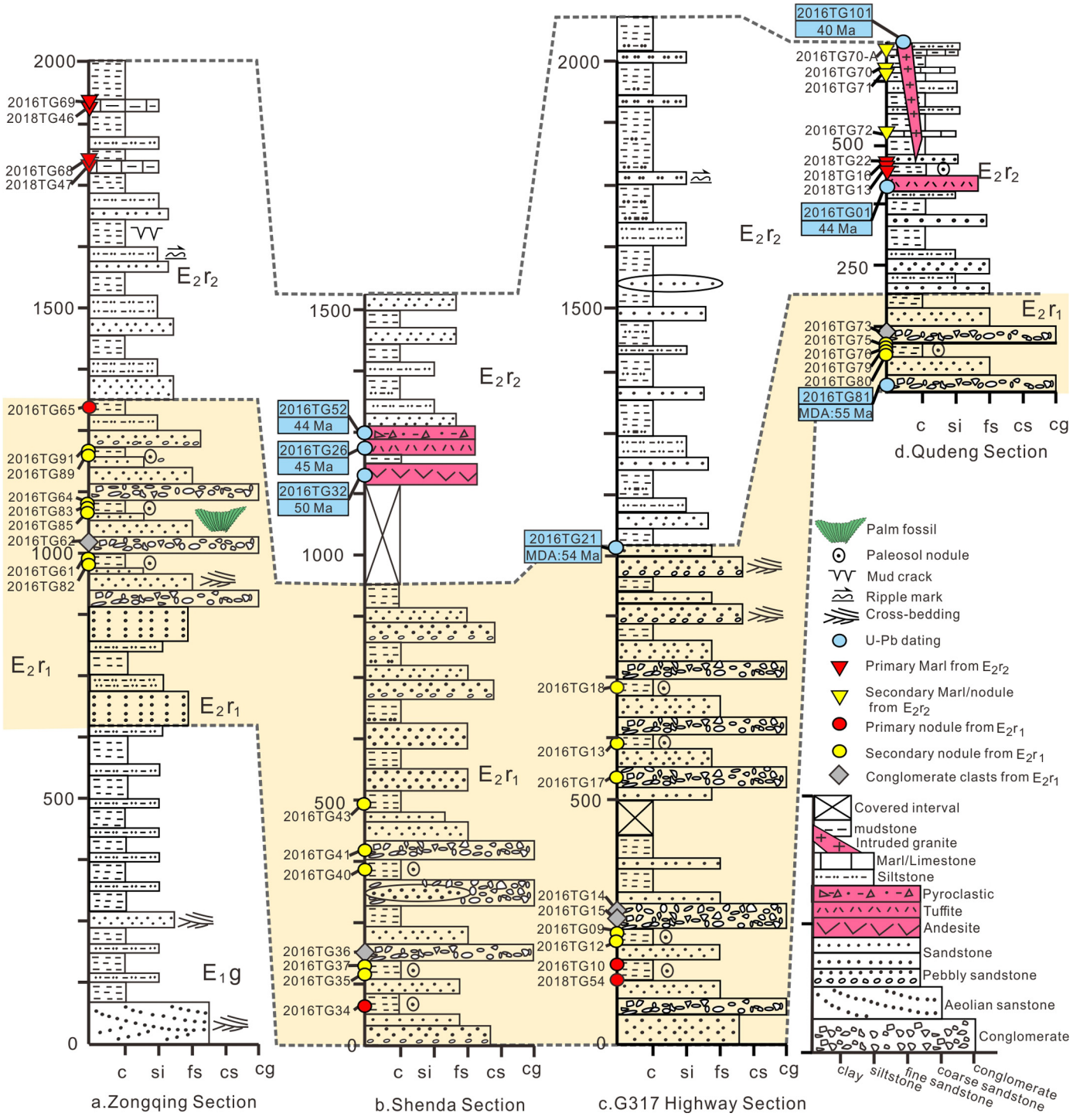

Fig. 3. Measured sections in the Gonjo Basin showing lithologies and samples taken for this study. Dashed lines show lithologic correlation among these sections. Locations of carbonate samples used for isotope analyses from E_2r_1 are marked with yellow and red circles while those from E_2r_2 are marked with yellow and red triangles, conglomerate clasts are marked by gray rectangles. U-Pb ages of volcanic rocks and sandstones are marked by blue circles, and the MDA values refer to maximum depositional age based on the youngest cluster of detrital U-Pb ages.

of three climate parameters: MAAT, lowest coldest quarter mean temperature (CQtrMT) and cold month mean temperature (CMMT) following the compilation of Reichgelt et al. (2018).

3.3. Carbonate stable isotope analysis

Oxygen and carbon isotopic compositions of the selected samples (refer to supplementary materials for methods of sampling and preparation) were determined using an IsoPrime100 gas source stable isotope ratio mass spectrometer equipped with a MultiPrep system at the Speleothem Laboratory, Institute of Earth Environment, Chinese Academy of Science. The resultant isotopic values of the carbonates are normalized to NBS-19 in conventional delta notation ($\delta^{18}O_c$ and $\delta^{13}C_c$) and are reported relative to VPDB with uncertainties better than 0.08‰ and 0.06‰ (2σ), respectively.

3.4. Carbonate clumped isotope analysis

The carbonate clumped isotope parameter Δ_{47} is defined as the deviation of isotopologues mass 47 relative to the amount expected for the stochastic distribution in CO_2 (Eiler, 2007). The analysis of Δ_{47} were conducted in the Key Laboratory of Cenozoic Geology and Environment, Institute of Geology and Geophysics, Chinese Academy of Sciences, following the method of Wang et al. (2016) (refer to supplementary materials for details of laboratory analysis and data deduction). We report standard error of replicates as external uncertainties of samples (1σ), but if the σ is smaller than the internal uncertainty, we replace it with the internal uncertainty (0.010‰). We employ the calibration of Zaarur et al. (2013) to convert our Δ_{47} data into temperature.

3.5. Isotope-enabled coupled atmosphere-ocean climate model

Stable isotope paleoaltimetry requires several assumptions regarding the source of moisture, recycling, and the atmospheric trajectory of moisture-laden airmasses that geologic data alone cannot conclusively constrain. We utilize HadCM3L-M2.1aD (2017), a coupled Atmosphere Ocean General Circulation model (AOGCM), with atmosphere and ocean isotopes included, to qualitatively constrain the moisture parameters underpinning our isotopic paleoaltimetry. The isotope model inherited the parameters used in Tindall et al. (2010), which accurately reproduces the modern spatial and temporal distribution of oxygen and deuterium isotopes (refer to supplementary materials for the setup of isotope-enabled coupled atmosphere-ocean climate model).

4. Results

4.1. Zircon U-Pb geochronology

The youngest zircon population of the sandstones collected from E_2r_1 was used to constrain the maximum depositional age (MDA) of the paleosol nodules in E_2r_1 via the weighted mean age of the youngest three grains that overlapped at 2σ[YC2σ(3+)] (Laskowski et al., 2019). The YC2σ(3+) for E_2r_1 from the G317 and Qudeng sections (2016TG21 and 2016TG81, Fig. 3c, 3d) are 53.8 ± 2.8 Ma and 54.6 ± 3.6 Ma, respectively (Fig. 4a). Three volcanic samples were collected from the lower part to the upper part of the E_2r_2 in the Shenda section, encompassing an andesite (2016TG32), a tuffite (2016TG26) and a pyroclastic rock (2016TG52) (Fig. 3b). The resultant zircon weighted mean $^{206}Pb/^{238}U$ ages of the three samples are 49.5 ± 0.3 Ma (1σ, MSWD = 0.78, $n = 19$), 45.5 ± 0.2 Ma (1σ, MSWD = 0.64, $n = 17$) and 44.3 ± 0.1 Ma (1σ, MSWD = 0.61, $n = 32$), respectively (Fig. 4b-d). The oldest age (50 Ma) of the andesite (2016TG32) in the E_2r_2 from the Shenda section constrained the minimum depositional age of the E_2r_1. The younger ages of the tuffite (2016TG26) and pyroclastic rock (2016TG32) in the E_2r_2 from the Shenda section are comparable to the zircon age of the tuffite sample (2016TG01) in the E_2r_2 from the Qudeng section (Fig. 3d), which give a weighted mean $^{206}Pb/^{238}U$ age of 44.2 ± 0.2 Ma (1σ, MSWD = 0.82, $n = 31$) (Fig. 4e). Therefore, we use the youngest age from the Shenda section and the tuffite age from the Qudeng section to constrain the lower limit of the sedimentary age of the carbonates in the E_2r_2. The granite (2016TG101, Fig. 3d) that intruded the sedimentary rocks of the basin yields an age of 40.1 ± 0.2 Ma (1σ, MSWD = 1.5, $n = 23$) (Fig. 4f), because the intrusion must be younger than the layers it cuts (i.e. the sedimentary age of E_2r_2), we use 40 Ma as the upper limit of the depositional age of the carbonates from E_2r_2. In summary, the sedimentary age of the paleosol nodules in E_2r_1 could be constrained to 54-50 Ma, and the sedimentary age of the paleosol nodules and marls in E_2r_2 could be constrained to 44-40 Ma.

4.2. Palm fossils

Palms are inherently cold sensitive (Reichgelt et al., 2018) and so make excellent paleoclimate proxies for determining maximum paleoelevation (Su et al., 2019). Three palm frond segments 14- to 40-cm-long (Fig. 2f) were preserved in parallel and likely belong to the same leaf. The fragments are single-folded, and the number of fold-segments in each fragment ranges from 3 to 5. These characteristics show that this specimen represents a pinnate palm (*Arecaceae*) leaf (refer to supplementary materials Fig. S2). Because the leaf fossil from the Gonjo Basin is pinnate, we use the climate ranges of subfamilies *Arecoideae*, *Ceroxyloideae*, *Nypoideae*, *Calamoideae* (tribe *Calameae*), and *Coryphoideae* (tribes *Caryoteae* and *Phoeniceae*) (Reichgelt et al., 2018), which also have pinnate leaves, to estimate conservatively the climate conditions under which the palm grew during the early Eocene of the Gonjo Basin. The lowest threshold for the MAAT was 9.1 °C, CQtrMT was 6.6 °C, and CMMT was 5.6 °C.

4.3. Carbon and oxygen isotopic results

In total, 27 of the 42 reworked Triassic marine limestone pebbles and cobbles collected in E_2r_1 yield $\delta^{18}O_c$ values between −8.0‰ and 0.0‰ (Fig. 5a, Supplementary material Table A3) (Veizer et al., 1999), the remaining limestone clasts give scattered $\delta^{18}O_c$ values ranging from −11.3‰ to −8.1‰.

The stable isotope composition of 34 authigenic carbonate samples are summarized as follows: The isotopic compositions for individual analysis of the paleosol nodules collected from E_2r_1 in the four sections encompass $\delta^{13}C_c$ values of −7.8‰ to −3.9‰, with an average value of −5.7 ± 1.2‰, and $\delta^{18}O_c$ values range from −14.1‰ to −7.7‰, with an average value of −10.5 ± 1.4‰ (Fig. 5a). The $\delta^{13}C_c$ values for individual analyses of paleosol nodules, marls and limestones collected from E_2r_2 range from −7.2‰ to −4.6‰, with an average value of −6.2 ± 0.6‰, and $\delta^{18}O_c$ values range from −16.6‰ to −9.1‰, with an average value of −14.7 ± 2.0‰ (Fig. 5a). The $\delta^{13}C_c$ and $\delta^{18}O_c$ values of E_2r_2 in four sections do not show obvious correlation (Fig. 5b). The $\delta^{18}O_c$ values of E_2r_1 show 3∼4‰ higher than those of E_2r_2. There is also a distinct difference in the $\delta^{13}C_c$ and $\delta^{18}O_c$ values between nodules from E_2r and the limestone clasts (Fig. 5a).

4.4. Clumped isotope temperatures ($T(\Delta_{47})$) results

Fourteen nodules from E_2r_1 have Δ_{47} values that range from 0.508 to 0.620 ‰ with $T(\Delta_{47})$ values ranging from 86 ± 4 °C to 27 ± 2 °C (1σ). Four samples have $T(\Delta_{47})$ values between 27 ± 2 °C and 36 ± 5 °C with a mean of 32 ± 4 °C (1σ, $n = 4$) (Fig. 6a), and the rest of the samples have relatively high $T(\Delta_{47})$ values between 43 ± 2 °C to 86 ± 4 °C (1σ) with a mean of 64 ± 16 °C(1σ, $n = 10$) (Fig. 6b).

Four out of five samples (micrites and nodules) from the E_2r_2 have Δ_{47} values range from 0.737 ‰ to 0.783 ‰ with $T(\Delta_{47})$ values ranging from 17 ± 4 °C to 8 ± 2 °C (1σ) (Fig. 6a), and the mean value is 12 ± 4 °C (1σ, $n = 4$). The $T(\Delta_{47})$ value of a limestone sample (2016TG71) is, abnormally, 30 °C higher than the micrites and nodules (Fig. 6b).

4.5. Climate modeling results

The Lutetian simulation predicts a slightly different climate to that of Modern observations (CMAP; Xie and Arkin, 1996) in the Gonjo Basin with Mean Annual Precipitation (MAP) for the Lutetian and Modern observations of 0.92 mm/day (Fig. 7a) and 1.41 mm/day, respectively. During the wet season (June, July, August - JJA) simulated Lutetian precipitation is also less than Modern day

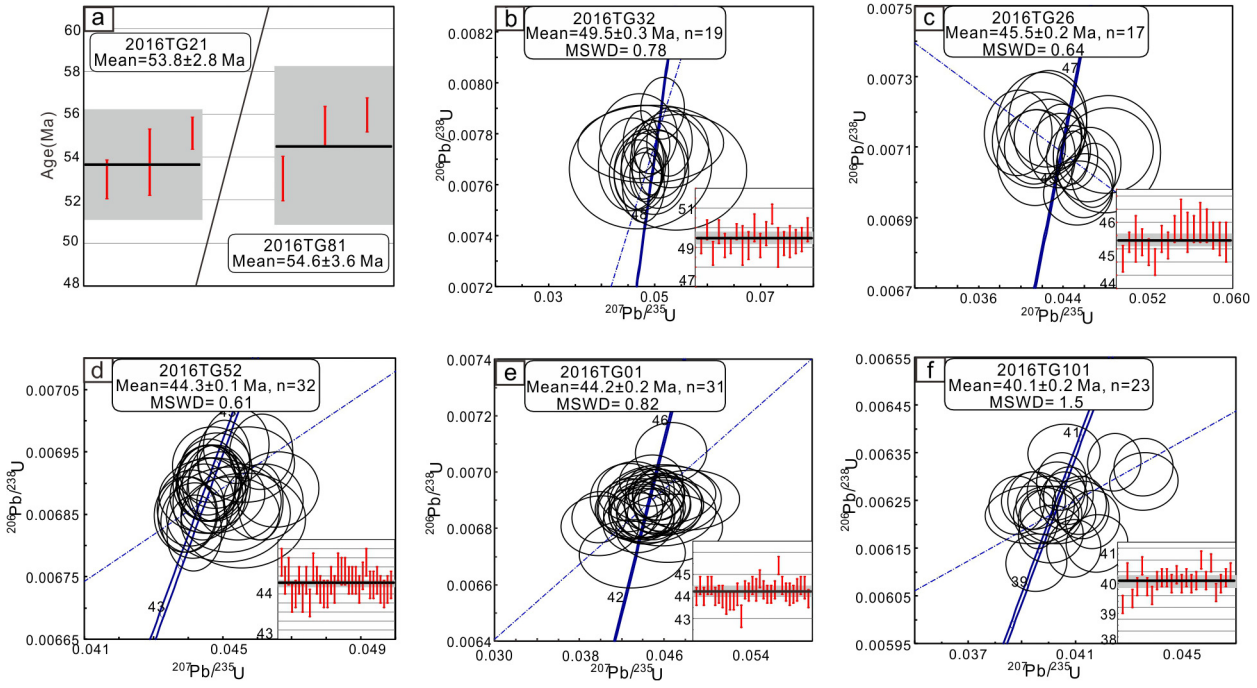

Fig. 4. LA-ICP-MS zircon U-Pb weighted mean averages and concordia diagrams of sandstones and volcanic rocks from the Gonjo Basin.

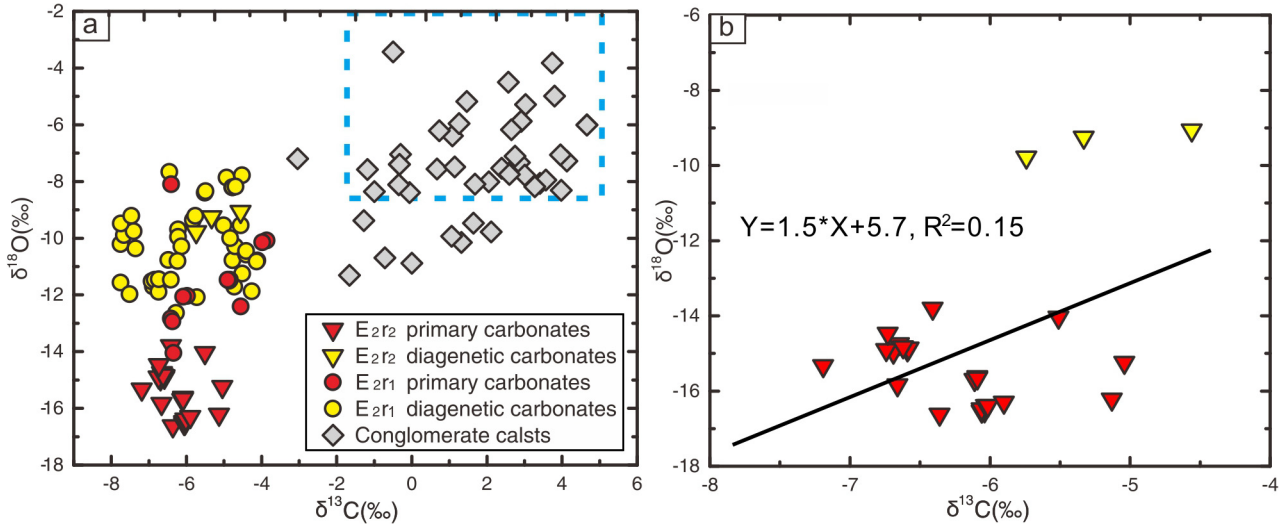

Fig. 5. (a) Cross-plot diagrams of the $\delta^{13}C$ and $\delta^{18}O$ values of carbonate samples and reworked Triassic limestone clasts from E_2r_1 and E_2r_2, blue dotted rectangle encompasses the $\delta^{18}O$ range of the Triassic limestone (Veizer et al., 1999). The differentiation of primary and diagenetic carbonates are determined by the $T(\Delta_{47})$ in section 5.1 to keep consistency of stable isotope data and $T(\Delta_{47})$ data. (b) Correlation of the $\delta^{13}C$ and $\delta^{18}O$ values of micrite from E_2r_2.

observations, being 0.51 mm/day and 3.33 mm/day, respectively (Xie and Arkin, 1996). Both simulated precipitation and Modern observations in the Gonjo Basin shows a strong seasonal signal dominated by summer (JJA) precipitation, however, the intensity when measured by a precipitation seasonality index as defined by Wang and Ding (2008) (Lutetian is 3.0 and modern day is 1.9, respectively) shows that the Lutetian precipitation was much more seasonal than today. The Lutetian JJA Precipitation in the Gonjo Basin has two sources, the dominant source of precipitation was from the proto-South China Sea region comprising a $\delta^{18}O$ composition of -6 ± 1‰, and a smaller source from the Paratethys with a $\delta^{18}O$ composition of -2 ± 1‰ (Fig. 7b). In winter (December, January, February - DJF), the Indian Ocean region and the Paratethys sources both have a $\delta^{18}O$ composition of -6 ± 1‰, together with a proto-South China Sea source of -2‰ to -4‰, but these are less significant considering the strong seasonality was dominated by summer precipitation.

5. Discussion

5.1. Diagenetic assessment

Post-depositional diagenesis such as recrystallization, fluid-rock interaction and solid-state reordering can overprint, sometimes strongly, the primary $\delta^{18}O_c$ values of carbonates, thus rendering the paleoelevation estimation meaningless (Garzione et al., 2004; Henkes et al., 2014). We employ clumped isotope thermometry coupled with petrographic analysis and the "conglomerate test" to evaluate the effects of diagenetic resetting.

Petrographic and elemental evaluation shows that the paleosol carbonates used in our paleoelevation calculation are mainly

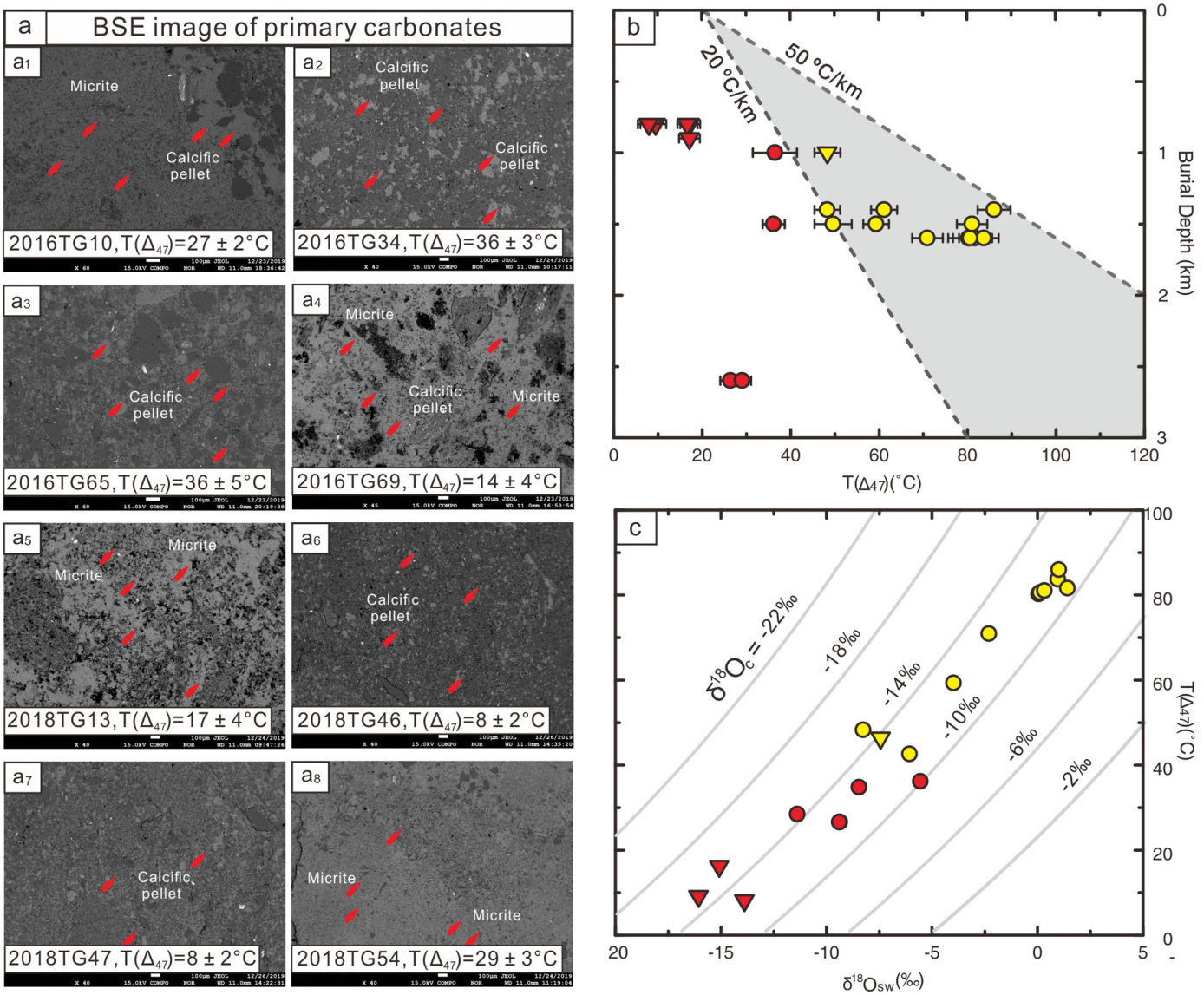

Fig. 6. (a) Backscatter (BSE) images of primary carbonates with $T(\Delta_{47})$. Red arrows denote the target points of element analysis. (b) Estimated burial depth versus $T(\Delta_{47})$. Filled circles and triangles show sample temperatures derived from carbonate clumped isotope data, the red circles and red triangles represent the primary formation temperatures of samples, and the yellow circles and triangles represent the diagenetic temperature of samples. The heavy dotted lines show estimated burial geotherms assuming an Earth surface temperature of 20 °C and a geothermal gradient of 20 °C/km to 50 °C/km. (c) Apparent oxygen isotope value of paleo-surface water ($\delta^{18}O_{sw}$) for the carbonate samples. We calculated $\delta^{18}O_{sw}$ values from which the carbonate precipitated with $\delta^{18}O_c$ and $T(\Delta_{47})$, following the fractionation equation of Kim and O'Neil (1997). The $\delta^{18}O_{sw}$ values are reported relative to VSMOW. Grey contours are solutions to the calcite-water oxygen isotope thermometry equations for constant $\delta^{18}O_c$ values.

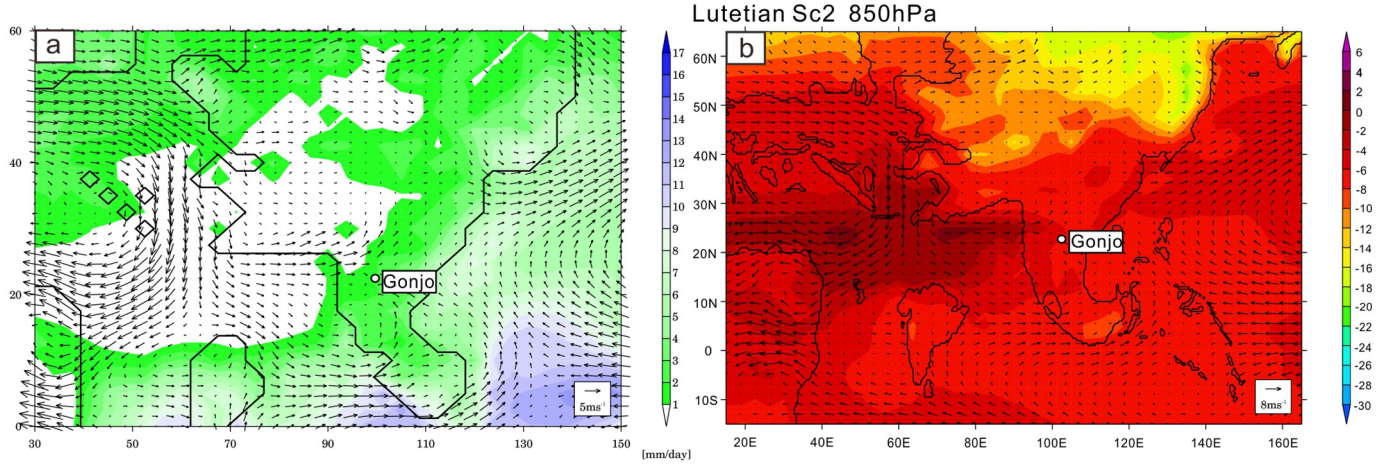

Fig. 7. Climate modeling results for the Lutetian. (a) Mean annual precipitation (mm/day), Wind vectors are overlain (m/s). (b) $\delta^{18}O$ of J-J-A precipitation.

calcareous micrite, without dolomite content, and barely contain sparry calcite within vug fills or veins (Fig. 6a, Supplementary materials Fig. S1, Table A2), so do not exhibit evidence of pervasive diagenesis. Marls are mainly calcareous microspar or micrite, some of which contain recrystallized ostracod fossils or fine laminae (Supplementary materials Fig. S1). The distinctive difference in carbon and oxygen isotope values between Triassic limestone clasts and paleosol carbonates in the "conglomerate test" (DeCelles et al., 2007) also indicates that the carbonates in the Gonjo Basin have not experienced pervasive post-depositional diagenesis (Fig. 5a).

However, microscale recrystallization and solid-state reordering may still exist without obvious change in the bulk isotopic composition or the texture of samples, the carbonate clumped isotope thermometer provides a further test for cryptic resetting. The formation temperature for modern surface carbonates in mid-latitude areas generally range below 40 °C (Burgener et al., 2016; Quade et al., 2013), and the $T(\Delta_{47})$ values in the Gonjo Basin should be consistent with the mid-latitude formation temperature, assuming they record the original condition of carbonates. The $T(\Delta_{47})$ of eight samples are within the range of Earth surface temperatures, while other samples have $T(\Delta_{47})$ over 40 °C. Although the difference in seasonality and soil depth at similar elevations could cause the $T(\Delta_{47})$ of carbonates to vary by 10-15 °C (Quade et al., 2013), it is still reasonable to suppose that samples with $T(\Delta_{47})$ over 40 °C have experienced diagenetic alteration due to the influence of the geothermal events.

Due to the lack of other independent constraints relevant to the thermal history of the basin, we apply fundamental geothermal evaluation to further identify possible diagenetic effects on samples. The burial depths of the carbonate samples in E_2r_1 and E_2r_2 were estimated according to the measured sections (Fig. 6b) (Studnicki-Gizbert et al., 2008). Assuming a normal geothermal gradient of 20–50 °C/km (Chen et al., 2013), the carbonate samples with $T(\Delta_{47})$ below 40 °C in E_2r_1 that were buried to depth of 3 km must have experienced burial temperatures from 80 °C to 170 °C. The effect of solid-state reordering is negligible when the burial temperature is below 100 °C, but will significantly increase the $T(\Delta_{47})$ to over 60 °C when burial temperature exceeds 110 °C (Henkes et al., 2014). Such a high temperature is far higher than the actual $T(\Delta_{47})$ of our samples. Combined with the warm climate revealed by the palm fossil, we interpret these $T(\Delta_{47})$ represent original sedimentary conditions. For other carbonate samples in E_2r_1 and E_2r_2, the effect of solid-state reordering with a burial temperature of 50–95 °C is negligible (Henkes et al., 2014). Therefore, the samples in E_2r_2 with $T(\Delta_{47})$ below 40 °C indicate primary depositional temperature while the rest samples are within the burial temperature range of the two units, respectively (Fig. 6b), and so the $T(\Delta_{47})$ from these samples may suggest recrystallization. The similarity of $\delta^{18}O_c$ values in the samples further indicates that the recrystallization occurred in a rock-buffered system (Fig. 6c). In summary, we consider the valid $T(\Delta_{47})$ for paleoelevation reconstruction in E_2r_1 ranges from 27 °C to 36 °C, with an average value of 32 ± 4 °C. The valid $T(\Delta_{47})$ for paleoelevation reconstruction in E_2r_2 ranges from 8 °C to 17 °C, with an average value of 12 ± 4 °C.

Quaternary soil carbonate in Tibet generally forms in the warmest months of the year when soil water becomes depleted, and the relationship between $T(\Delta_{47})$ and MAAT is understood (Quade et al., 2013). The distinct difference between wet and dry seasons from climate modeling indicates a hotter and more arid SE Tibet in the Eocene than present, thus the E_2r_1 nodules might also have formed in the late spring and autumn, and the difference between the $T(\Delta_{47})$ and MAAT should be smaller (Gallagher and Sheldon, 2016). Due to the depth within the Eocene Gonjo Basin soil profile being unknown, we use the correlation of $T(\Delta_{47})$ to MAAT without correction for soil depth in Quade et al. (2013). On this basis, the calculated MAAT in the early Eocene Gonjo Basin is ~24 ± 4 °C, which is consistent with the warm climate revealed by the palm fossil. For the middle Eocene micrites, we use the empirical transfer relationship between the mean lake surface temperature and MAAT in the Northern Hemisphere spring (Hren and Sheldon, 2012), and obtain the MAAT in the middle Eocene Gonjo Basin of ~7 ± 4 °C. The present MAAT of the Gonjo Basin is 6.5 °C, which is similar with the calculated middle Eocene MAAT of the Gonjo Basin.

5.2. Evaporation

Evaporation in lakes leads to the enrichment of heavy isotopes in lacustrine sediments. Therefore, the assessment of possible evaporation enrichment is of critical importance in validating our paleoelevation results. A combination of $\delta^{18}O_c$ distribution and the analysis of $\delta^{18}O_c$ versus $\delta^{13}C_c$ covariance can be used to indicate evaporation-induced enrichment in carbonates (Talbot, 1990). The $\delta^{18}O_c$ values of marls and mudstones from the upper part of E_2r_2 range from −16.62‰ to −9.06‰, with an R of 0.4, and so were likely to have been deposited in a stable open lacustrine environment with a relatively short residence time (Talbot, 1990).

5.3. Calculation of paleoelevation

Oxygen isotope paleoaltimetry has been widely used for estimating the paleoelevation of the Tibetan region (e.g. Ding et al., 2014; Rowley and Currie, 2006; Xu et al., 2013). By exploiting the relationship between the isotopic differences in precipitation between sea level and higher elevations ($\Delta(\delta^{18}O_{mw})$) due to Rayleigh fractionation processes, Rowley et al. (2001) constructed a thermodynamics-based model to determine past surface elevation. Our climate modeling results of the Lutetian also show strong seasonal changes in both precipitation and low-level wind (850 hPa) fields (Fig. 7), indicating the presence of a summer monsoonal climate affecting SE Tibet in the Eocene, which is comparable to the modern precipitation pattern (Li and Garzione, 2017; Valdes et al., 2019). This monsoonal climate is consistent with leaf architectural signals, ostracod and gastropod shells evidence that suggest a pervasive monsoonal climate has influenced South Asia since at least the late Eocene (Ding et al., 2014; Licht et al., 2014; Spicer et al., 2016). These lines of evidence indicate the dominant moisture source in the Eocene over SE Tibet was the ocean to the south of Asia, and followed a similar Rayleigh fractionation process to that seen in SE Tibetan Plateau today, even though the pattern and intensity of Eocene precipitation were not exactly same.

Temperatures derived independently from carbonate clumped isotope thermometry record the formation temperature of primary carbonates and can therefore be used to obtain accurate oxygen isotope values of the paleo-surface water ($\delta^{18}O_{sw}$). The calculated $\delta^{18}O_{sw}$ values of the E_2r_1 range between −10.8‰ and −5.6‰ with an average value of −8.5 ± 0.3‰ (1σ), while those of the E_2r_2 are between −17.1‰ and −14.8‰ with an average value of −15.6 ± 0.7‰ (1σ).

In the Rayleigh fractionation model, the $\delta^{18}O_{sw}$ values must be corrected for latitudinal and continental effects. Paleomagnetic evidence indicates that the Qiangtang Terrane was at a paleolatitude of ~29°N in the Late Cretaceous, and so ~3° latitude lower than its present position (Chen et al., 2017). Assuming the same condition for the early Eocene Gonjo Basin, the 3° latitudinal difference exerts an enrichment effect of +0.3‰ on the precipitation compared to its modern counterpart (Bowen and Wilkinson, 2015). However, regional crustal shortening and rotation took place during the middle Eocene (Spurlin et al., 2005; Tong et al., 2017) suggest negligible latitudinal effect on precipitation of the E_2r_2. The continental effect relates to the oxygen isotope value of the

source water vapor becoming more depleted as it passes over a continent (Dansgaard, 1964). To calibrate the continental effect on precipitation falling in the Eocene Gonjo Basin, we assume the effect was analogous to that of the modern Alps in Europe, i.e., approximately −2.0‰/1000 km (Winnick et al., 2014), and this is consistent with the Lutetian isotope-enabled climate model with a simulated gradient of −1.92‰/1000 km across Asia (Fig. 7). We use the modern distance (400 km) between the Gonjo Basin and the Yalung-Zangpo suture zone to provide a minimum constraint on $\delta^{18}O_{sw}$ (i.e. −0.8‰).

The $\delta^{18}O$ value of the moisture source is also required before applying the Rayleigh fractionation model. The oxygen isotope values of planktonic and benthic foraminifers from the low latitude oceans during the early Paleogene indicate the sea surface temperature in these oceans remained constant and within the range of Holocene temperatures (Zachos et al., 1994), so we assume the sea surface temperature of the source ocean exerts minimal effect on the isotopic composition of precipitation. Accounting for continental ice sheet development since the late Eocene, the $\delta^{18}O$ value of the present sea water is approximately +1.2‰ richer than that in the Eocene (Zachos et al., 1993, 2001). Therefore, we applied a correction of −1.2‰ to the average $\delta^{18}O$ value (−5.9‰) of GNIP stations of South Asia coastal cities (New Delhi, Yangon, Dhaka, Hanoi, Sylhet and Guangzhou) and obtained a value of −7.1 ± 1‰ for the Eocene oxygen isotope composition of the moisture source. The isotope-enabled ocean-atmosphere climate model for the Lutetian indicates most of the precipitation within the Gonjo Basin was carried by the summer monsoon from the ocean to the south of Asia, with only a minor contribution from the Paratethys. The source of the precipitation from the southern monsoon has a value of −6 ± 1‰, which is consistent with our assumption regarding the oxygen isotope composition of the moisture source.

When bring these parameters into the model, $\Delta(\delta^{18}O_{sw})$ from the E_2r_1 paleosol carbonates in the early Eocene is −1.1 ± 0.4‰, and those from E_2r_2 lacustrine carbonates and paleosol carbonates in the middle Eocene is −8.0 ± 1.3‰ (Fig. 8a). The calculated paleoelevation of the E_2r_1 in the early Eocene is ∼0.7 (+0.8/−0.9) km (Fig. 8a). The thermal constraints of the palm found in the Zongqing section corroborates the relatively low elevation of the E_2r_1. The corresponding paleoelevation of the E_2r_2 in the middle Eocene is ∼3.8 (+0.8/−1.1) km (Fig. 8a), which is comparable with the present elevation of the Gonjo Basin. The uncertainties reported in the paleoelevation are propagated uncertainties inclusive of the low elevation precipitation source, variation from the $\delta^{18}O_c$, $T(\Delta_{47})$ and the Rayleigh fractionation model (Rowley et al., 2001; Li et al., 2018).

The modern near-surface air temperature lapse rate (TLR) of the Tibetan Plateau during the summer time range from −4.6 °C/km to −7.3 °C/km, with an averaged value of −5.9 °C/km. The TLRs increase in dry and cold conditions, but decrease in humid and warm conditions (Guo et al., 2016). Therefore, it is appropriate to assume the mean TLR of the present Tibetan Plateau provides a first-order constraint on the uplift history of the Eocene Gonjo Basin. The MAAT of the Gonjo Basin (24 ± 4 °C) in the early Eocene is higher than that (7 ± 4 °C) of the middle Eocene by 17 °C. After applying 2 °C to correct the global temperature cooling between the early and middle Eocene (Zachos et al., 2001), the Gonjo Basin rose about 2.9 (+0.8/−0.5) km between the early and middle Eocene with a TLR of −5.9 °C/km. Because of the markedly warmer climate in the early Eocene Gonjo Basin, our calculation just gives a minimum surface rise. The surface uplift derived from oxygen isotope paleoaltimetry (3.1 km) and temperature lapse rate (2.9 km) are comparable, and indicate a rapid rise of the Gonjo Basin, from a relatively low elevation to a near present elevation between the early and middle Eocene.

Comparing our paleoelevation results for the early Eocene Gonjo Basin with the 2.1-2.5 km estimate in the previous study of Tang et al. (2017), their paleoelevation seems to be overestimated by 1.4–1.8 km. The overestimation could be due to the use of an inaccurate carbonate formation temperature derived from the MAAT in the nearby Litang Basin. The MAAT in the Litang Basin was obtained using Leaf Margin Analysis (LMA), which has been shown to be unreliable, particularly in monsoon climates (Yang et al., 2015). When compared to our $T(\Delta_{47})$, the temperature derived from the LMA underestimates the formation temperature of soil carbonates by 7 °C, and therefore results in a 1.5‰ depletion in $\delta^{18}O_{sw}$, so falsely increasing their calculated surface height by 1.4–1.8 km.

According to our elevation results, the Gonjo Basin was at relatively low elevation (∼0.7 km) during the early Eocene (54-50 Ma) and rose to high elevation (∼3.8 km) in the middle Eocene (44-40 Ma). These estimates indicate the Gonjo Basin experienced a surface uplift of ∼3.1 km between the early and middle Eocene.

5.4. Implications for the regional topography and tectonic processes

Combined with previous elevation data from the Lhasa and Qiangtang terranes, we have developed a tentative paleotopographic framework for Paleocene-Eocene Tibet. The paleoelevations of the Linzhou and Namling basins in the southern Lhasa Terrane indicate the formation of a high Andean-type Gangdese mountain range during Paleocene-Eocene time (Ding et al., 2014; Ingalls et al., 2018), and Ding et al. (2014) infer that the uplift of the central Qiangtang Terrane probably coincided with, or occurred immediately after, the rise of the Gangdese mountain range (Fig. 8b, 9a). The high elevation of the Gonjo Basin in the middle Eocene is consistent with the high elevations of the Paleogene Heihuling, Nangqian and Markam basins (Fig. 8b) (Li et al., 2018; Su et al., 2018; Xu et al., 2013). The rapid exhumation of central and SE Tibet between 60-40 Ma derived from thermochronological evidence is comparable with those high paleoelevation estimates (Rohrmann et al., 2012; Liu-Zeng et al., 2018). These pieces of evidence suggest that the Qiangtang Terrane was uplifted during the Paleocene to Eocene, beginning in its central part and then propagated eastwards, at which point the high elevation of the Central Watershed mountain range formed. Moreover, the Liming and Jianchuan basins, thought to be the eastern extension of the paleo-Qiangtang Terrane, might have attained high elevations before the Miocene (Hoke et al., 2014). In contrast, the fossil evidence from the Lunpola and Nima basins suggest the existence of a lowland region, during the Paleogene (Su et al., 2019; Wu et al., 2017). Therefore, the topography of Tibet during the Eocene primarily consisted of two high east-west aligned mountain ranges (The Gangdese and the Central Watershed) bounding a low-elevation valley: the paleo-Lunpola-Nima Basin (Fig. 9b).

The rapid Eocene rise of the Gonjo Basin has implications regarding the forces responsible for its uplift. The high elevation of the Gangdese mountain range and the central part of the Central Watershed mountain range during the early Eocene, indicate that the crust of the Lhasa and Qiangtang terranes was already thickened due to the subduction and detachment of the Neo-Tethyan oceanic slab (Ding et al., 2014; Kapp and DeCelles, 2019; Xu et al., 2013) (Fig. 9a). The development of Paleogene thrust systems in the central Qiangtang Terrane indicate that continental subduction was the primary mechanism driving the significant contraction and shortening in the central Qiangtang Terrane (Kapp et al., 2005). The northward subduction of India promoted the detachment of the Neo-Tethyan lithospheric mantle in the middle Eocene (Fig. 9a). The detachment of Neo-Tethyan lithospheric mantle further initiated intracontinental subduction between the Lhasa and Qiangtang terranes (Ding et al., 2007). The Qiangtang crust is weaker than that of the Lhasa crust due to the existence of the underthrust

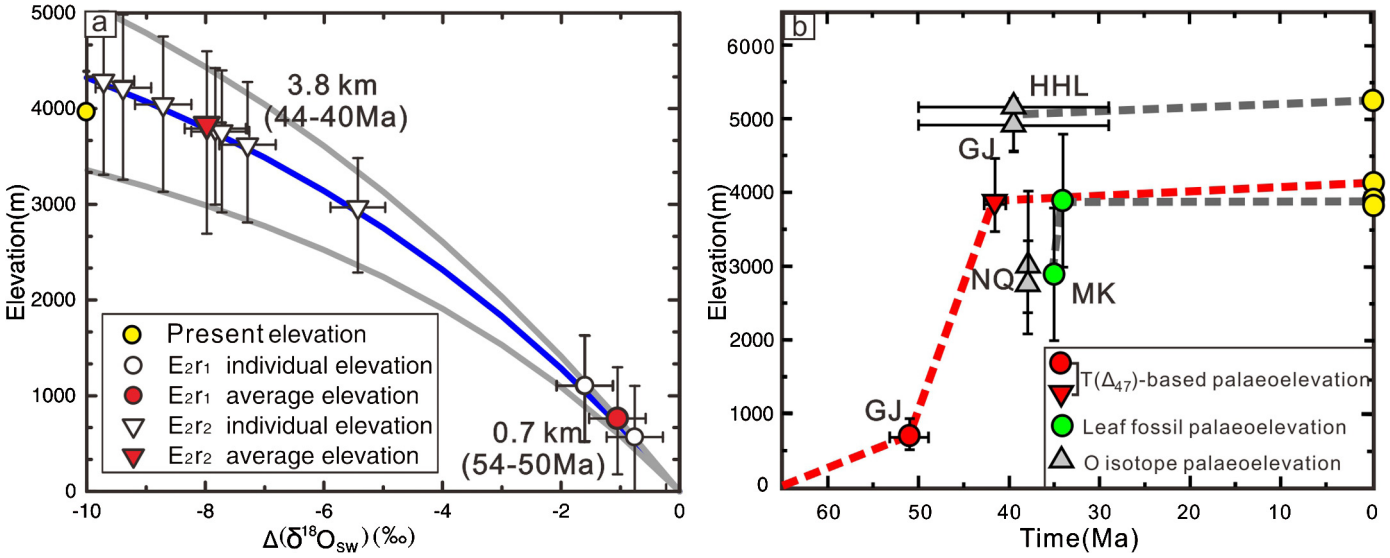

Fig. 8. Predicted paleoelevations of the Gonjo Basin and time-elevation plot for the Qiangtang Terrane. (a) The $\Delta(\delta^{18}O_{sw})$ values derived from carbonates yield an average elevation of 0.7 km for the early Eocene E_2r_1 and an average elevation of 3.8 km for the middle Eocene E_2r_2. (b) For the Qiangtang Terrane, the paleoelevations of the Gonjo Basin in the early and middle Eocene in this study are denoted by the red circle and the red triangle, respectively. Previous oxygen isotope-based paleoelevations from Paleogene Heihuling Basin and Eocene Nangqian Basin are denoted by grey triangles (Li et al., 2018; Xu et al., 2013), while results derived from plant fossil in the late Eocene Markam Basin are denoted by green circles (Su et al., 2018). The present elevations of those basins are denoted as yellow circles.

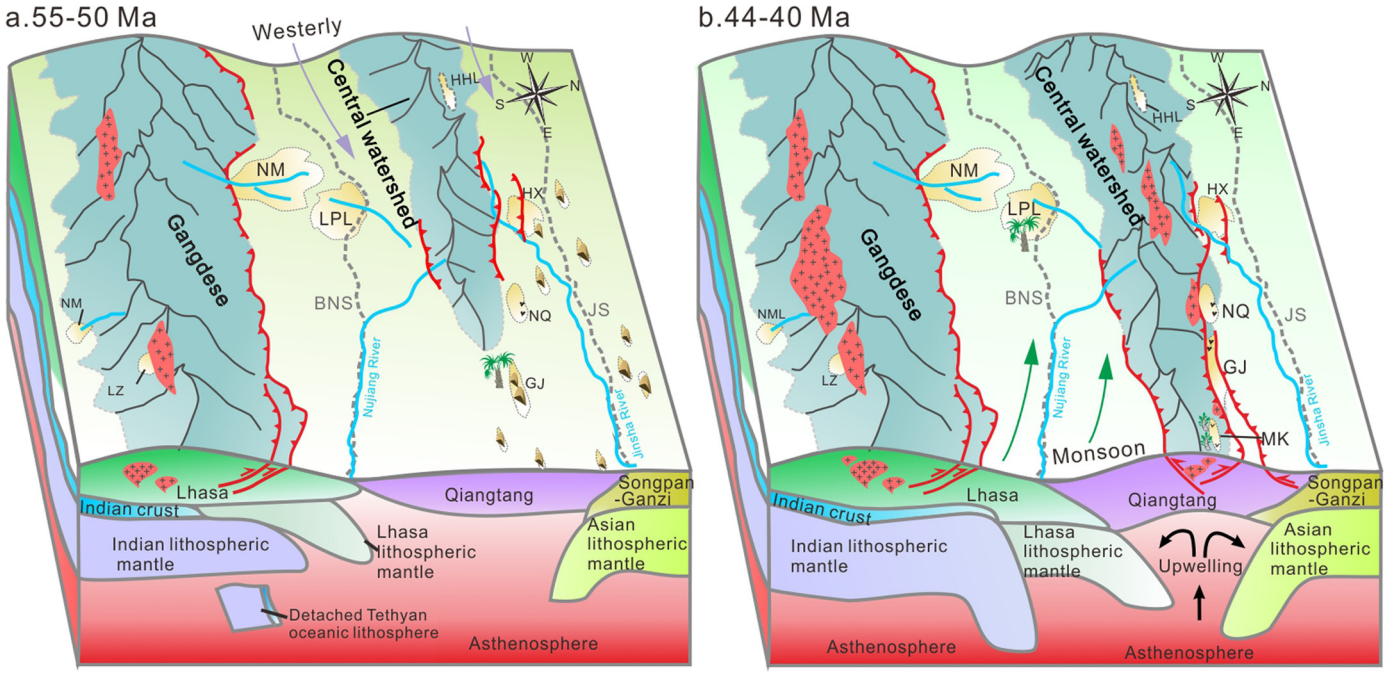

Fig. 9. Block model illustrating the development of the Central Watershed mountain range in the Qiangtang Terrane. (a) Between 55-50 Ma, the Gangdese mountain range in the Lhasa Terrane had already formed as a high Andean-type mountain range with an elevation over 4.5 km (Ding et al., 2014). The Central Watershed mountain range rose to high elevation in the central Qiangtang Terrane while the eastern Qiangtang Terrane was at low elevation and receiving dominantly eolian sedimentation. At depth, the subduction of the Neo-Tethyan oceanic slab promoted the growth of the Gangdese mountain range, and subsequent detachment of the Neo-Tethyan oceanic slab initiated the underthrust of the Lhasa Terrane to the Qiangtang Terrane (Kapp et al., 2005). (b) Between 44-40 Ma, the growth of the Central Watershed mountain range developed to the eastern Qiangtang Terrane, and the Nangqian, Gonjo, Markam basins have risen to high elevation. The paleo-Lunpola-Nima Basin stood at low elevation (Su et al., 2019). Combined with high Gangdese mountain range, the topography of Tibet formed as two high mountain ranges that sandwiched a low-land valley (Ding et al., 2014; Su et al., 2019). The cause of the rapid uplift of the Central Watershed mountain range may be due to crustal deformation and thickening that induced by intracontinental subduction between the Lhasa and Qiangtang terranes. Heat advection in the mantle induced pervasive magmatism in the Qiangtang Terrane (Ding et al., 2007).

mélange, thus the Qiangtang Terrane is more prone to deformation (Kapp et al., 2005). This resulted in considerable lateral crustal deformation and the rapid uplift of the Central Watershed mountain range (Fig. 9b). As the effects of the collision between India and Asia moved progressively to eastern Tibet, the intracontinental subduction and the corresponding continental shortening of the Lhasa and Qiangtang terranes were also gradually accommodated in central Tibet and spread to SE Tibet (Ding et al., 2017; Kapp et al., 2005). The Early Paleogene thin-skinned thrusting along the Fenghuoshan-Yushu-Nangqian thrust belt indicates that deformation propagated to the eastern Qiangtang Terrane (Spurlin et al., 2005; Staisch et al., 2016). Two parallel zones of Paleocene to Oligocene magmatism with contrasting compositions within the Qiangtang Terrane suggest heat advection resulting from intra-

continental subduction rather than convective removal of mantle lithosphere (Ding et al., 2007).

5.5. Implications for paleoclimate

An Asian Eocene monsoonal climate has been proposed based on the strong seasonality of $\delta^{18}O_c$ in mammal teeth, ostracod and gastropod shells from Tibet and Myanmar, and leaf architecture signatures from Eocene basins in southwestern China (Ding et al., 2014; Licht et al., 2014; Spicer et al., 2016). The temperature derived from $T(\Delta_{47})$ indicates a MAAT of 24 $\pm$ 4 °C in the Gonjo Basin during the early Eocene, which was relatively warm. The existence of eolian deposits in E_1g and the palm vegetation in E_2r_1 are consistent with warm and semi-arid conditions. Conversely, the low MAAT (7 $\pm$ 4 °C) of E_2r_2 reveals the Gonjo Basin experienced a transition from a warm and generally arid climate to a relatively cold and presumably forest-supporting climate during the early Eocene as the growth of the Central Watershed mountain range developed progressively eastward from the central Qiangtang Terrane to the eastern Qiangtang Terrane. The temperate evergreen vegetation in the Markam Basin, and sedimentological data from the Jianchuan Basin, document the plant cover and relatively humid conditions within SE Tibet in the late Eocene (Sorrel et al., 2017; Su et al., 2018). These lines of evidence indicate that the development of the Asian Eocene monsoon was coeval with the rise of the Gangdese and the Central Watershed mountain ranges, so we infer the Eocene monsoonal climate over this part of the Tibetan region is dominantly a response to orographic development rather than global climate forcing (Bosboom et al., 2014). This is also supported by climate modeling that reveals the Ancient Asian monsoon was controlled by paleogeography, not CO_2 (Farnsworth et al., 2019). In response to topographic change, the monsoonal climate vectored the moisture from South Asia into the plateau interior and triggered biological transition across the SE Tibet during the Eocene (Spicer et al., 2016; Su et al., 2018; Xie et al., 2019).

6. Conclusion

This study provides well age-constrained clumped isotope-based paleoelevation estimates from the Eocene Gonjo Basin. The paleoelevation data indicate that the Gonjo Basin was at a relatively low elevation (~0.7 km) during the early Eocene (54-50 Ma), and then rose rapidly to ~3.8 km in the middle Eocene (44-40 Ma). The low elevation and the existence of palm fossil and eolian sediment in the early Eocene Gonjo Basin and other Eocene basins within the Qiangtang Terrane (Horton et al., 2002), indicate the region was dominated by a low elevation desert climate in the early Eocene. The present high elevation of the Gonjo Basin was achieved by the middle Eocene, and combined with the paleoelevation records of the Qiangtang Terrane and the northern Lanping-Simao Terrane (Hoke et al., 2014; Li et al., 2018; Su et al., 2018; Xu et al., 2013), suggests much of the northern part of SE Tibet has been at high elevation since the middle Eocene, and that the Central Watershed mountain range of the Qiangtang Terrane has existed since then. Crustal deformation and thickening induced by intracontinental subduction between the Lhasa and Qiangtang terranes was the main cause for the middle Eocene rapid uplift of the Gonjo Basin. Triggered by the topographic uplift of the Gangdese and the Central Watershed mountain ranges in the Eocene, the climate in the SE Tibet also changed from a desert climate to one with a stronger monsoonal influence.

Declaration of competing interest

We declare that we have no conflict of interest.

Acknowledgements

We are grateful to Feng Cheng, Lin Li and an anonymous reviewer for their detailed and constructive comments which greatly improved the quality of the manuscript. Editor An Yin is thanked for handling this manuscript. This work was supported by the National Natural Science Foundation of China (Grant No. 41490615); the National Key Research and Development Project of China (Grant No. 2016YFC0600303); the Chinese Academy of Sciences, Strategic Priority Research Program (Grant No. XDA20070301); Second Tibetan Plateau Scientific Expedition and Research Program (Grant No. 2019QZKK0708); the National Natural Science Foundation of China (Grant No. 41941016, 41661134049); Natural Environment Research Council of the UK (NE/P013805/1, NE/K014757/1, NE/I005722/1 and NE/I005714/1). We also thanked S.L. He and D. Zeng for their field assistance, and J.X. Zhai and B. Qin for their help in measuring carbonate clumped isotopes.

Appendix A. Supplementary material

Supplementary material related to this article can be found online at https://doi.org/10.1016/j.epsl.2020.116312.

References

Bosboom, R.E., Abels, H.A., Hoorn, C., et al., 2014. Aridification in continental Asia after the middle Eocene climatic optimum (MECO). Earth Planet. Sci. Lett. 389, 34–42.
Bowen, G.J., Wilkinson, B., 2015. Spatial distribution of $\delta^{18}O$ in meteoric precipitation. Geology 30, 315–318.
Burchfiel, B.C., Chen, Z., 2012. Tectonics of the southeast Tibetan Plateau and its adjacent foreland. Mem. Geol. Soc. Amer. 210, 1–164.
Burgener, L., Huntington, K.W., Hoke, G.D., et al., 2016. Variations in soil carbonate formation and seasonal bias over >4 km of relief in the western Andes (30°S) revealed by clumped isotope thermometry. Earth Planet. Sci. Lett. 441, 188–199.
Chen, H., Wu, Y., Xiao, Q., 2013. Thermal regime and paleogeothermal gradient evolution of Mesozoic-Cenozoic sedimentary basins in the Tibetan Plateau, China. Earth Sci., J. China Univ. Geosci. 38, 541–552.
Chen, W., Zhang, S., Ding, J., et al., 2017. Combined paleomagnetic and geochronological study on Cretaceous strata of the Qiangtang terrane, central Tibet. Gondwana Res. 41, 373–389.
Clark, M.K., House, M.A., Royden, L.H., et al., 2005. Late Cenozoic uplift of southeastern Tibet. Geology 33, 525–528.
Clark, M.K., Royden, L.H., 2000. Topographic ooze: building the eastern margin of Tibet by lower crustal flow. Geology 28, 703–706.
Dansgaard, W., 1964. Stable isotopes in precipitation. Tellus 16, 436–468.
DeCelles, P.G., Quade, J., Kapp, P., et al., 2007. High and dry in central Tibet during the late Oligocene. Earth Planet. Sci. Lett. 253, 389–401.
Deng, J., Wang, Q., Li, G., Santosh, M., 2014. Cenozoic tectono-magmatic and metallogenic processes in the Sanjiang region, southwestern China. Earth-Sci. Rev. 138, 268–299.
Ding, L., Maksatbek, S., Cai, F.L., et al., 2017. Processes of initial collision and suturing between India and Asia. Sci. China Earth Sci. 60, 635–651.
Ding, L., Kapp, P., Yue, Y., Lai, Q., 2007. Postcollisional calc-alkaline lavas and xenoliths from the southern Qiangtang terrane, central Tibet. Earth Planet. Sci. Lett. 254, 28–38.
Ding, L., Xu, Q., Yue, Y., et al., 2014. The Andean-type Gangdese mountains: paleoelevation record from the Paleocene-Eocene Linzhou basin. Earth Planet. Sci. Lett. 392, 250–264.
Eiler, J.M., 2007. "Clumped-isotope" geochemistry-the study of naturally-occurring, multiply-substituted isotopologues. Earth Planet. Sci. Lett. 262, 309–327.
Farnsworth, A., Lunt, D.J., Robinson, S.A., et al., 2019. Past East Asian monsoon evolution controlled by paleogeography, not CO_2. Sci. Adv. 5. eaax1697.
Friedman, G.M., Sanders, J.E., 1978. Principles of Sedimentology. Wiley, New York.
Gallagher, T.M., Sheldon, N.D., 2016. Combining soil water balance and clumped isotopes to understand the nature and timing of pedogenic carbonate formation. Chem. Geol. 435, 79–91.
Garzione, C.N., Dettman, D.L., Horton, B.K., 2004. Carbonate oxygen isotope paleoaltimetry: evaluating the effect of diagenesis on paleoelevation estimates for the Tibetan Plateau. Palaeogeogr. Palaeoclimatol. Palaeoecol. 212, 119–140.
Gourbet, L., Leloup, P.H., Paquette, J., et al., 2017. Reappraisal of the Jianchuan Cenozoic basin stratigraphy and its implications on the SE Tibetan Plateau evolution. Tectonophysics 700, 162–179.
Guo, X., Wang, L., Tian, L., 2016. Spatio-temporal variability of vertical gradients of major meteorological observations around the Tibetan Plateau. Int. J. Climatol. 36, 1901–1916.

Henkes, G.A., Passey, B.H., Grossman, E.L., et al., 2014. Temperature limits for preservation of primary calcite clumped isotope paleotemperatures. Geochim. Cosmochim. Acta 139, 362–382.
Hren, M.T., Sheldon, N.D., 2012. Temporal variations in lake water temperature: paleoenvironmental implications of lake carbonate $\delta^{18}O$ and temperature records. Earth Planet. Sci. Lett. 337–338, 77–84.
Hoke, G.D., Liu-Zeng, J., Hren, M.T., Wissink, G.K., Garzione, C.N., 2014. Stable isotopes reveal high southeast Tibetan Plateau margin since the Paleogene. Earth Planet. Sci. Lett. 394, 270–278.
Horton, B.K., Spurlin, M.S., Zhou, J.Y., Wang, J.H., 2002. Paleocene-Eocene syncontractional sedimentation in narrow, lacustrine-dominated basins of East-central Tibet. Geol. Soc. Am. Bull. 114, 771–786.
Ingalls, M., Rowley, D., Olack, G., 2018. Paleocene to Pliocene low-latitude, high-elevation basins of southern Tibet: implications for tectonic models of India-Asia collision, Cenozoic climate, and geochemical weathering. Geol. Soc. Am. Bull. 130, 307–330.
Kapp, P., DeCelles, P.G., 2019. Mesozoic-Cenozoic geological evolution of the Himalayan-Tibetan orogen and working tectonic hypotheses. Am. J. Sci. 319, 159–254.
Kapp, P., Yin, A., Harrison, T.M., Ding, L., 2005. Cretaceous-Tertiary shortening, basin development, and volcanism in central Tibet. Geol. Soc. Am. Bull. 117, 865–878.
Kim, S.T., O'Neil, J.R., 1997. Equilibrium and nonequilibrium oxygen isotope effects in synthetic carbonates. Geochim. Cosmochim. Acta 61, 3461–3475.
Laskowski, A.K., Orme, D.A., Cai, F., Ding, L., 2019. The ancestral Lhasa river: a late Cretaceous trans-arc river that drained the proto-Tibetan Plateau. Geology 47, 1029–1033.
Licht, A., Van, C.M., Abels, H.A., et al., 2014. Asian monsoons in a late Eocene greenhouse world. Nature 513, 501–506.
Li, L., Fan, M., Davila, N., Jesmok, G., Mitsunaga, B., Tripati, A., Orme, D., 2018. Carbonate stable and clumped isotopic evidence for late Eocene moderate to high elevation of the East-central Tibetan Plateau and its geodynamic implications. Geol. Soc. Am. Bull. 131, 831–844.
Li, L., Garzione, C.N., 2017. Spatial distribution and controlling factors of stable isotopes in meteoric waters on the Tibetan Plateau: implications for paleoelevation reconstruction. Earth Planet. Sci. Lett. 460, 302–314.
Li, S., Currie, B.S., Rowley, D.B., Ingalls, M., 2015. Cenozoic paleoaltimetry of the SE margin of the Tibetan Plateau: constraints on the tectonic evolution of the region. Earth Planet. Sci. Lett. 432, 415–424.
Linnemann, U., Su, T., Kunzmann, L., et al., 2017. New U-Pb dates show a Paleogene origin for the modern Asian biodiversity hot spots. Geology 46, 3–6.
Liu-Zeng, J., Zhang, J., Mcphillips, D., et al., 2018. Multiple episodes of fast exhumation since Cretaceous in southeast Tibet, revealed by low-temperature thermochronology. Earth Planet. Sci. Lett. 490, 62–76.
Quade, J., Eiler, J., Daëron, M., Achyuthan, H., 2013. The clumped isotope geothermometer in soil and paleosol carbonate. Geochim. Cosmochim. Acta 105, 92–107.
Reichgelt, T., West, C.K., Greenwood, D.R., 2018. The relation between global palm distribution and climate. Sci. Rep. 8, 4721.
Rohrmann, A., Kapp, P., Carrapa, B., et al., 2012. Thermochronologic evidence for plateau formation in central Tibet by 45 Ma. Geology 40, 187–190.
Rowley, D.B., Currie, B.S., 2006. Palaeo-altimetry of the late Eocene to Miocene Lunpola basin, central Tibet. Nature 439, 677–681.
Rowley, D.B., Pierrhubert, R.T., Currie, B.S., 2001. A new approach to stble isotope-based paleoaltimetry: implications for paleoaltimetry and paleohypsometry of the High Himalaya since the Late Miocene. Earth Planet. Sci. Lett. 188, 253–268.
Royden, L.H., Burchfiel, B.C., Van der Hilst, R.D., 2008. The geological evolution of the Tibetan Plateau. Science 321, 1054–1058.
Schenk, C.J., Fryberger, S.G., 1988. Early diagenesis of eolian dune and interdune sands at White Sands, New Mexico. Sediment. Geol. 55, 109–120.
Searle, M.P., 2006. Role of the Red River Shear zone, Yunnan and Vietnam, in the continental extrusion of SE Asia. J. Geol. Soc. 163 (6), 1025–1036.
Sorrel, P., Eymard, I., Leloup, P.H., et al., 2017. Wet tropical climate in SE Tibet during the Late Eocene. Sci. Rep. 7, 7809.
Spicer, R.A., Yang, J., Herman, A.B., et al., 2016. Asian Eocene monsoons as revealed by leaf architectural signatures. Earth Planet. Sci. Lett. 449, 61–68.
Spicer, R.A., Harris, N.B.W., Widdowson, M., et al., 2003. Constant elevation of southern Tibet over the past 15 million years. Nature 421, 622–624.
Spurlin, M.S., Yin, A., Horton, B.K., Zhou, J., Wang, J., 2005. Structural evolution of the Yushu-Nangqian region and its relationship to syncollisional igneous activity, East-central Tibet. Geol. Soc. Am. Bull. 117, 1293–1317.
Staisch, L.M., Niemi, N.A., Clark, M.K., Chang, H., 2016. Eocene to late oligocene history of crustal shortening within the Hoh Xil basin and implications for the uplift history of the northern Tibetan Plateau. Tectonics 35, 862–895.
Studnicki-Gizbert, C., Burchfiel, B.C., Li, Z., Chen, Z., 2008. Early Tertiary Gonjo basin, eastern Tibet: sedimentary and structural record of the early history of India-Asia collision. Geosphere 4, 713–735.
Su, T., Spicer, R.A., Li, S., et al., 2018. Uplift, climate and biotic changes at the Eocene-Oligocene transition in Southeast Tibet. Nat. Sci. Rev. nwy062.
Su, T., Farnsworth, A., Spicer, R.A., et al., 2019. No high Tibetan Plateau until the Neogene. Sci. Adv. 5. eaav2189.
Talbot, M.R., 1990. A review of the palaeohydrological interpretation of the carbon and oxygen isotopic ratios in primary lacustrine carbonates. Chem. Geol. 80, 261–279.
Tang, M., Liu-Zeng, J., Hoke, G.D., et al., 2017. Paleoelevation reconstruction of the Paleocene-Eocene Gonjo basin, SE-central Tibet. Tectonophysics 712–713, 170–181.
Tapponnier, P., Xu, Z.Q., Roger, F., et al., 2001. Oblique stepwise rise and growth of the Tibetan Plateau. Science 294, 1671–1677.
Tindall, J., Flecker, R., Valdes, P., et al., 2010. Modelling the oxygen isotope distribution of ancient seawater using a coupled ocean-atmosphere GCM: implications for reconstructing early Eocene climate. Earth Planet. Sci. Lett. 292, 265–273.
Tong, Y., Yang, Z., Mao, C., et al., 2017. Paleomagnetism of Eocene red-beds in the eastern part of the Qiangtang Terrane and its implications for uplift and southward crustal extrusion in the southeastern edge of the Tibetan Plateau. Earth Planet. Sci. Lett. 475, 1–14.
Valdes, P.J., Lin, Ding, Farnsworth, A., et al., 2019. Comment on "Revised paleoaltimetry data show low Tibetan Plateau elevation during the Eocene". Science 365. eaax8474.
Veizer, J., Ala, D., Azmy, K., et al., 1999. $^{87}Sr/^{86}Sr$, $\delta^{13}C$ and $\delta^{18}O$ evolution of Phanerozoic seawater. Chem. Geol. 161, 59–88.
Wang, B., Ding, Q.H., 2008. Global monsoon: dominant mode of annual variation in the tropics. Dyn. Atmos. Ocean. 44, 165–183.
Wang, X., Cui, L., Li, Y., et al., 2016. Determination of clumped isotopes in carbonate using isotope ratio mass spectrometry: toward a systematic evaluation of a sample extraction method using a static Porapak™ Q absorbent trap. Int. J. Mass Spectrom. 403, 8–14.
Winnick, M.J., Chamberlain, C.P., Caves, J.K., Welker, J.M., 2014. Quantifying the isotopic 'continental effect'. Earth Planet. Sci. Lett. 406, 123–133.
Wu, F., Miao, D., Chang, M.M., Shi, G., Wang, N., 2017. Fossil climbing perch and associated plant megafossils indicate a warm and wet central Tibet during the late Oligocene. Sci. Rep. 7, 878.
Xie, P., Arkin, P.A., 1996. Analyses of global monthly precipitation using gauge observations, satellite estimates, and numerical model predictions. J. Climate 9, 840–858.
Xie, Y., Wu, F., Fang, X., 2019. Middle Eocene East Asian monsoon prevalence over southern China: evidence from palynological records. Glob. Planet. Change 175, 13–26.
Xu, Q., Ding, L., Zhang, L., et al., 2013. Paleogene high elevations in the Qiangtang Terrane, central Tibetan Plateau. Earth Planet. Sci. Lett. 362, 31–42.
Xu, Z., Wang, Q., Cai, Z., et al., 2015. Kinematics of the Tengchong Terrane in SE Tibet from the late Eocene to early Miocene: insights from coeval mid-crustal detachments and strike-slip shear zones. Tectonophysics 665, 127–148.
Yang, J., Spicer, R.A., Spicer, T.E.V., et al., 2015. Leaf form-climate relationships on the global stage: an ensemble of characters. Glob. Ecol. Biogeogr. 10, 1113–1125.
Yin, A., Harrison, T.M., 2000. Geological evolution of the Himalayan-Tibetan orogen. Annu. Rev. Earth Planet. Sci. 28, 211–280.
Zaarur, S., Affek, H.P., Brandon, M.T., 2013. A revised calibration of the clumped isotope thermometer. Earth Planet. Sci. Lett. 382, 47–57.
Zachos, J.C., Lohmann, K.C., Walker, J.C.G., Wise, S.W., 1993. Abrupt climate change and transient climates in the Paleogene: a marine perspective. J. Geol. 101, 193–215.
Zachos, J., Pagani, M., Sloan, L., Thomas, E., Billups, K., 2001. Trends, rhythms, and aberrations in global climate 65 Ma to present. Science 292, 686–693.
Zachos, J.C., Stott, L.D., Lohmann, K.C., 1994. Evolution of early Cenozoic marine temperatures. Paleoceanography 9, 353–387.
Zhang, B., Chai, Z., Yin, C.Y., et al., 2017. Intra-continental transpression and gneiss doming in an obliquely convergent regime in SE Asia. J. Struct. Geol. 97, 48–70.